Journal of Computational Physics 229 (2010) 361–378

Contents lists available at ScienceDirect

Journal of Computational Physics

journal homepage: www.elsevier.com/locate/jcp

TOKAM-3D: A 3D fluid code for transport and turbulence in the edge plasma of Tokamaks

P. Tamain [a,*], Ph. Ghendrih [a], E. Tsitrone [a], V. Grandgirard [a], X. Garbet [a], Y. Sarazin [a], E. Serre [b], G. Ciraolo [b], G. Chiavassa [b]

[a] *Association Euratom-CEA, Institut de Recherche sur la Fusion Magnétique, CEA Cadarache, F-13108 St. Paul-lez-Durance, France*
[b] *Laboratoire M2P2-UMR-6181 La Jete Technople de Chateau-Gombert 38, Rue F. Joliot Curie-13451, Marseille Cedex 20, France*

ARTICLE INFO

Article history:
Received 19 August 2008
Received in revised form 26 June 2009
Accepted 22 September 2009
Available online 30 September 2009

PACS:
47.11.Bc
47.27.−E
52.30.Ex
52.35.Ra

Keywords:
Modelling
Tokamak
Edge plasma
Transport
Turbulence

ABSTRACT

We present a new code aiming at giving a global and coherent approach for transport and turbulence issues in the edge plasma of Tokamaks. The *TOKAM-3D* code solves 3D fluid drift equations in full-torus geometry including both closed field lines and SOL physics. No scale separation is assumed so that interactions between large scale flows and turbulence are coherently treated. Moreover, the code can be run in transport regimes ranging from purely anomalous diffusion to fully established turbulence. Specific numerical schemes have been developed which can solve the model equations whether the presence of a limiter in the plasma is taken into account or not. Example cases giving an overview of the field of application of the code as well as verification results are also presented.

1. Introduction

Plasma–wall interaction [1] is one of the key issues to be addressed in ITER on the route towards making magnetic fusion a viable energy source. In this field of research, turbulent cross-field transport bridges all the physics at hand. Among the key issues that still require considerable effort are the radial width of the heat channel at the plasma boundary-as well as its generalisation to density and momentum-the physics of the onset of the H-mode edge transport barrier, the physics that governs the density limit and last but not least the operation of a divertor in a detached plasma regime. While the latter issue clearly involves a lot of atomic physics, the three first issues appear to be strongly related to the underlying cross-field transport.

Furthermore, it appears that this problem cannot be properly addressed if the key geometrical property of this region, namely the existence of a domain of closed field lines, the edge plasma, and the neighbouring domain of open field lines, referred to as the Scrape-Off Layer (SOL), are not addressed together and on the same footing. In that framework, the

* Corresponding author. Present address: EURATOM/UKAEA Fusion Association, Culham Science Centre, Abingdon, Oxon OX14 3DB, UK. Tel.: +44 123546 6602.
E-mail address: patrick.tamain@ukaea.org.uk (P. Tamain).

0021-9991/$ - see front matter © 2009 Elsevier Inc. All rights reserved.
doi:10.1016/j.jcp.2009.09.031

existence of large scale flows generated by both the magnetic equilibrium and the plasma turbulence are also observed to play an important role in this interface region [2]. Other experimental [3,4] and theoretical studies [5,6] suggest that turbulence and transport properties are dramatically different in the core and in the SOL. The physics taking place at the interface between these two layers, ie in the vicinity of the Last Closed FLux Surface (LCFS), is still under investigation. This issue is all the more important as several fundamental open questions are linked to this area, such as the H-mode pedestal formation [7,8] or the so-called spontaneous rotation of the core plasma [9].

A large palette of tools have been developed to address transport and turbulence issues in the edge plasma of Tokamaks. These codes have helped clarifying our understanding of basic phenomena involved in edge physics. However, important questions remain little explored due to limitations in the field of application of most of these tools: transport models [10–13] require ad-hoc transport coefficients as an input although this approach is not necessarily valid [14,15]; 2D turbulence models [16–18] cannot give an insight on the parallel dynamics of turbulence since they rely on the flute hypothesis on which recent results shed doubt [19]; gradient-driven models [20] require hypotheses on plasma equilibrium profiles or coupling with transport codes and do not reproduce the whole richness of multiscale dynamics [19]; exclusive closed field lines [21] or SOL [16] codes are not able to take coherently into account the physics linked to the open-closed field lines transition across the LCFS... Some of these limitations can be overcome by coupling several codes together [22–24], but a part of the physics can be lost in the process.

In the last few years, a lot of effort has been put in the development of advanced tools to overcome those limitations [25–27]. The aim of this paper is introduce a new edge code aiming at giving a global and coherent approach for edge transport and turbulence issues. The *TOKAM-3D* code solves 3D electrostatic fluid drift equations in a full-torus geometry with no scale separation and is able to cover both closed and open flux surfaces accross the LCFS. Furthermore, *TOKAM-3D* can be run in a continuum of transport regimes ranging from purely diffusive transport to fully developed turbulence, by simply adding an ad-hoc level of diffusive transport on top of turbulent transport equations. The physics currently included in the code remains simpler than what is treated in more advanced tools like BOUT [25] or GEM [28], but the project is bound to be further developed. Our purpose here is to present the physical model, its numerical implementation as well as first numerical results illustrating validations and the range of applications.

The remainder of this paper is organized as follows. In the next section, the *TOKAM-3D* model is derived. Particular attention is given to the geometry and boundary conditions which are key features of the code. The numerical implementation of the model is described in Section 3. Two slightly different schemes are presented, corresponding to two different versions of the code. One treats only edge closed flux surfaces and takes advantage of the double periodicity of the geometry in that case, while the other is able to cover both closed and open flux surfaces. Finally, Section 4 illustrates the field of application of the code with simple simulations in the different regimes and geometries the code can handle. The presented cases also provide basic verifications of the code's behaviour and accuracy.

2. Physical model

2.1. 3D full-torus geometry in limiter configuration

We consider a plasma confined by a magnetic field in Tokamak geometry. Toroidal coordinates (r,θ,φ) and the associated local orthonormal base $(\vec{e}_r,\vec{e}_\theta,\vec{e}_\varphi)$ are used (Fig. 1). Toroidal limiter configuration has been chosen and flux surfaces are axisymmetric tori with concentric circular poloidal cross-sections. This choice greatly simplifies the treatment without sacrificing the main features of edge physics (particle sources and sinks, electrostatic potential regulation via sheath currents, loss of periodicity along the poloidal direction). Moreover, such geometrical assumptions are close to the actual situation on some Tokamaks, like Tore Supra. Since neutrals are not modelled, the main limitation imposed by not considering an X-point divertor geometry is the absence of the strong poloidally localized magnetic shear that both affects the spreading of turbu-

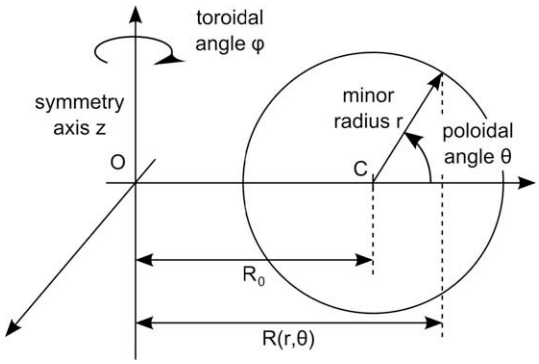

Fig. 1. Definition of toroidal coordinates.

lence and flows across the LCFS and isolates the main SOL from the divertor legs [29]. X-point resistivity driven modes [30] are also not considered.

Let R_0 be the major radius on the magnetic axis and a be the minor radius at the LCFS. Fig. 2 illustrates the adopted geometry. The computational domain is a toroidal ring delimited by flux surfaces $r = r_{\min}$ and $r = r_{\max}$. The inner radius is located in the closed flux surfaces region ($r_{\min} < a$). Concerning the outer radius $r_{\max}$, two situations must be distinguished:

- If $r_{\max} > a$, the simulated region extends into the SOL characterized by the presence of the limiter which "opens" the field lines and therefore breaks the periodicity. The limiter fills a poloidal angular section $\Delta_{\lim}$ at the bottom of the machine ($\theta \in [-\pi/2 - \Delta_{\lim}/2; -\pi/2 + \Delta_{\lim}/2]$) for $r \in]a, r_{\max}]$.
- Otherwise, $r_{\max} = a$ and the simulated region is bounded by the LCFS.

This way, *TOKAM-3D* can be run in two different geometries corresponding to slightly different sets of boundary conditions, depending on whether the simulated region crosses the LCFS and covers the SOL or not. We will talk about "edge" and "edge/SOL" versions of the code to designate each case.

The magnetic equilibrium is entirely defined by the specification of a safety factor profile $q(r)$ and of an amplitude $B(r,\theta)$ at each poloidal location. Since the code currently addresses electrostatic turbulence, fluctuations of the magnetic field are neglected and the magnetic configuration is constant. Assuming a large aspect ratio $A = R_0/a \gg 1$, we can define the small parameter $\epsilon_B = \frac{r}{qR_0} \ll 1$. The magnetic field is then given at the first order in ϵ_B by:

$$\vec{B} = B(r,\theta)\vec{b} \approx B(r,\theta)\begin{pmatrix} 0 \\ \epsilon_B \\ 1 \end{pmatrix} \tag{1}$$

with

$$B(r,\theta) = \frac{1}{1 + \frac{r}{R_0}\cos\theta} \tag{2}$$

Note that the amplitude is equal to one on the magnetic axis $r = 0$ due to the chosen normalization convention.

2.2. Fluid approach

The will to derive our model without scale separation makes it necessary to adopt a flux-driven approach for turbulence, either by volume sources or by fluxes at the boundary. To insure its coherency, simulations must be run for long times, typically several confinement times τ_E, so that the system can reach a consistent equilibrium. The range of frequencies to be treated is therefore:

$$\tau_E^{-1} \lesssim \omega \lesssim \gamma_{\max} \tag{3}$$

where $\gamma_{\max}$ is the growth rate of most unstable modes. Typical values in a medium-sized machine like Tore Supra are $\tau_E^{-1} \approx 10\ \mathrm{s}^{-1}$ and $\gamma_{\max} \approx 2 \times 10^6\ \mathrm{s}^{-1}$. Concerning spatial scales, perpendicular gradient lengths $k_\perp^{-1}$ range from the smallest scale of turbulence $l_\perp$ to the major radius of the machine R_0:

$$l_\perp \lesssim k_\perp^{-1} \lesssim R_0 \tag{4}$$

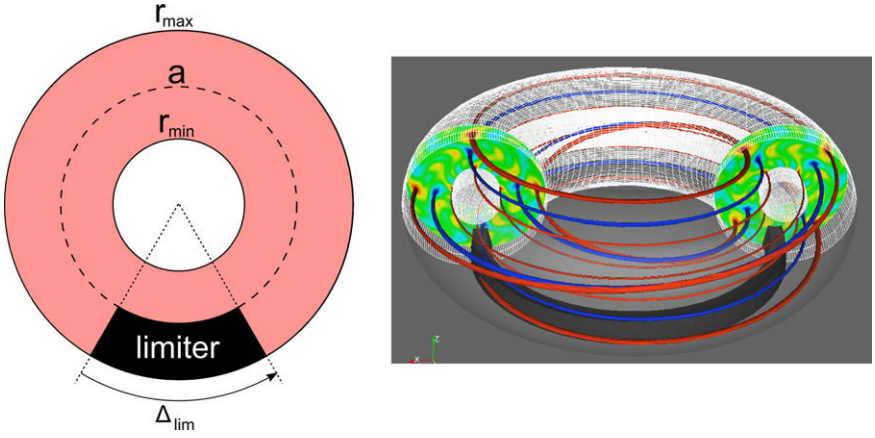

Fig. 2. Axisymmetric geometry used in the *TOKAM-3D* code. Left: poloidal cross-section; the colored area corresponds to the simulated region. Right: 3D toroidal view.

with typical values of $R_0 \approx 3$ m and $l_\perp \sim \rho_L \approx 5 \times 10^{-4}$ m for a deuterium plasma in the vicinity of the LCFS (the ion gyro-radius ρ_L appears as the natural lower scale for ion turbulence since smaller structures would not influence the ion dynamics due to the gyro-averaging along their trajectory).

In such conditions, the spatial mesh necessary to describe with full resolution 10 cm in the radial direction around the LCFS of a Tokamak of the size of Tore Supra ($a = 0.7$ m so $\rho^*_{edge} = \rho_L/a \sim 1 \times 10^{-3}$) would require $N_r \sim 2^7$ radial points, $N_\theta \sim 2^{12}$ poloidal points and $N_\varphi \sim 2^8$ toroidal points, which makes a total of $2^{27} \sim 10^8$ degrees of freedom per field for the only spatial dimensions. The use of field-aligned coordinates would substantially reduce the total resolution and is considered for future developments.

Although present computing means and their constant evolution allow the use of gyrokinetic modelling on such meshes, we have adopted a less demanding fluid approach for our model. This choice can be justified for plasma conditions in SOLs where high density and low temperature make the particle mean free path smaller than the parallel connection length of field lines to the wall. However, the theoretical validity of the fluid approach is more questionable in hot low density SOLs or inside the LCFS where the mean free path rises along with the temperature profile and non-Maxwellian distribution functions can arise from radial mixing. However, fluid models, even out of their formal validity domain, allow one to get a qualitative insight on the main physical mechanisms underlying turbulence and transport physics.

2.3. 3D fluid drift equations

TOKAM-3D solves two-fluid balance equations [31] under drift approximation, following the same approach as Ref. [32]. Four equations are derived, leading to evolution equations for four unknown dimensionless fields: the electronic density N, the electrostatic potential Φ, the ion parallel velocity M_T and the parallel current $J_\parallel$. These equations are the following:

$$\partial_t N + B\nabla_\parallel \frac{NM_T}{B} - B\nabla_\parallel \frac{J_\parallel}{B} + \frac{1}{B}[\Phi, N] = -BN\left[\Phi, \frac{1}{B^2}\right] + B\left[N, \frac{1}{B^2}\right] + \vec{\nabla}_\perp \cdot \left(D_{\perp N}\vec{\nabla}_\perp N\right) + S_N \tag{5}$$

$$\partial_t M_T + M_T\nabla_\parallel M_T + \frac{1}{B}[\Phi, M_T] = -(1+Z)\frac{\nabla_\parallel N}{N} + \vec{\nabla}_\perp \cdot \left(D_{\perp M_T}\vec{\nabla}_\perp M_T\right) - \frac{S_N}{N}M_T + S_M \tag{6}$$

$$\partial_t W + M_T\nabla_\parallel W + \frac{1}{B}[\Phi, W] = Z\frac{B^3}{N}\nabla_\parallel \frac{J_\parallel}{B} + (1+Z)\frac{B^3}{N}\left[N, \frac{1}{B^2}\right] + \vec{\nabla}_\perp \cdot \left(D_{\perp W}\vec{\nabla}_\perp W\right) \tag{7}$$

$$\eta_\parallel N J_\parallel = \nabla_\parallel N - N\nabla_\parallel \Phi \tag{8}$$

where the vorticity W is defined by

$$W = \nabla^2_\perp \Phi + \frac{\nabla^2_\perp \ln N}{Z} \tag{9}$$

Isothermal closure is presently assumed for electronic and ionic temperatures, $T_e = T_i = T_0 = 1$ (normalized value). Hence, this first version of the code does not integrate mechanisms like sheath-driven electron temperature-gradient modes or temperature driven flows. Energy balance equations are already planned to be added in future versions of the code.

All quantities are normalized with respect to the ions gyro-motion. The magnetic field amplitude on the magnetic axis $B(r = 0)$ is chosen as the reference magnetic field amplitude B_0 as well as the temperature of the isothermal plasma T_0. This way, one can define a gyro-frequency and a gyro-radius:

$$\omega_{ci} = \frac{eB_0}{m_i}\rho_L = \frac{\sqrt{m_i T_0}}{eB_0} \tag{10}$$

which are used to normalize the time and lengths. The electrostatic potential Φ is normalized to T_0/e while the density is normalized to an arbitrary reference N_0. All the other normalization conventions are derived from the previous ones.

Eqs. (5)–(8) share the same structure. They express the temporal variation of any local quantity X as the sum of local driving source terms and of the divergence of its total flux $\vec{\Gamma}_X$ which can be decomposed as the combination of a convective flux and a diffusive one:

$$\vec{\Gamma}_X = X\vec{V} - \mathbb{D}_X\vec{\nabla}X \tag{11}$$

The parallel component of the advection velocity $\vec{V}\cdot\vec{b}$ is defined by M_T for the ions and by $J_\parallel$ for the electrons. Under the drift approximation, the perpendicular components are described in terms of drifts according to a development in $\epsilon_\omega = \omega/\omega_{ci} \ll 1$ (ω_{ci} being the ion gyro-frequency) of the perpendicular momentum balance equation:

$$\vec{V} = V_\parallel\vec{b} + \vec{V}_E + \vec{V}_\star + \vec{V}_p \tag{12}$$

The electric drift velocity $\vec{V}_E = (\vec{B}\wedge\vec{\nabla}\Phi)/B^2$ and the diamagnetic drift velocity $\vec{V}_\star = (\vec{B}\wedge\vec{\nabla}(n_sT_s))/(q_sn_sB^2)$ (where n_s, T_s and q_s are the density, the temperature and the charge of the considered particles species, ions or electrons in our case) are taken into account for both ions and electrons, while the second order polarization velocity $\vec{V}_p = \frac{m_s}{q_sB^2}\vec{B}\wedge[\partial_t + (V_\parallel\vec{b} + \vec{V}_E).\vec{\nabla}](\vec{V}_E + \vec{V}_\star)$, linked to inertia effects, is kept only for ions when it appears under a divergence operator (as in [32]).

The electron balance Eq. 5 includes the divergence of the parallel, ExB drift and diamagnetic fluxes. The latter gives a curvature term representing the effect of the particle curvature drift velocity. The notation $[X,Y]$ stands for the Poisson bracket operator:

$$[X,Y] = \left(\vec{\nabla}X \wedge \vec{\nabla}Y\right) \cdot \vec{b} \tag{13}$$

while $\nabla_{\parallel} = \vec{b}.\vec{\nabla}$ is the projection of the gradient along the local direction of the magnetic field. A volumic source term S_N is also included to drive the particle flux.

Eq. 6 is the parallel momentum balance in which advection by ExB drift and parallel velocity is taken into account. It has been combined with the electron balance equation to obtain an equation of evolution for the normalized parallel velocity M_T. No advection by the diamagnetic drift velocity appears due to its cancellation with finite gyro-radius terms from the Braginskii pressure tensor (classical result known as diamagnetic cancellation [33]). The driving term is the parallel pressure gradient $(1+Z)\nabla_{\parallel}\ln N$, with Z the charge of the considered ion species. Note that, due to the chosen normalization, the dimensionless ionic parallel velocity M_T is linked to the parallel Mach number M by:

$$M_T = \sqrt{\frac{T_e + T_i}{T_0}} \cdot M = \sqrt{2} \cdot M \tag{14}$$

S_M is a momentum source to account for external momentum input (via neutral beam injection for example).

The vorticity evolution Eq. 7 determines the evolution of the electrostatic potential Φ. It is simply a charge balance under quasi-neutrality assumption $\vec{\nabla} \cdot \vec{j} = 0$, with $\vec{j} = J_{\parallel}\vec{b} + N(\vec{V}^i_{\star} - \vec{V}^e_{\star}) + N\vec{V}_p$. The vorticity terms (left hand side) arise from the divergence of the polarization current, while the diamagnetic current is responsible for the curvature term.

Finally, Eq. 8 is the electrons motion equation along parallel direction neglecting electronic inertia. It leads to a generalized Ohm's law linking the parallel current $J_{\parallel}$ to the parallel gradients of density and potential. $\eta_{\parallel}$ is the normalized parallel collisional resistivity of the plasma. Neglecting the electron inertia limits the scope of the code to frequencies lower than the electron collision frequency, equal to a few micro-seconds in typical SOL conditions.

Diffusion terms account for collisional and viscous transport and help to damp small turbulent scales that could be lethal for the code. The damping of scales smaller than the ion Larmor radius can be justified by physics considerations on the gyro-averaging during the ions motion since we only consider frequencies $\omega \ll \omega_{ci}$. Diffusion terms can also be set to larger values to account for an arbitrary level of diffusive transport, such as neoclassical or anomalous transport. Their parallel component is neglected compared with parallel convection so that we keep only perpendicular diffusion. They are characterized by constant but space-dependent diffusion coefficients $D_{\perp N/M/W}(r,\theta)$. Even though they are scalar by default, they can be locally different along the radial and poloidal directions in buffer regions (see Section 2.4).

2.4. Boundary conditions

The two versions of the code treat two different geometries and have therefore two different sets of boundary conditions. We shall now detail them for each version.

2.4.1. Boundary conditions in the edge version

In the edge version, flux surfaces are closed so that all fields are periodic along the poloidal and toroidal directions (θ,φ):

$$\forall r,\theta,\varphi \quad X(r,\theta+2\pi,\varphi) = X(r,\theta,\varphi) \quad \text{and} \quad X(r,\theta,\varphi+2\pi) = X(r,\theta,\varphi) \tag{15}$$

X standing for any considered field.

Radial boundary conditions aim mainly at controlling entering and outgoing fluxes and currents so as to insure a coherent flux-driving of the system by the only volumic sources $S_{N/M}$. At the inner flux surface ($r = r_{\min}$), we impose:

$$\begin{aligned} &\partial_r N(r_{\min}) = 0; \quad M(r_{\min}) = M_{\text{core}} \\ &\partial_r \Phi(r_{\min}) = 0; \quad \partial_r W(r_{\min}) = 0 \end{aligned} \tag{16}$$

where M_{core} is an arbitrary imposed value for the parallel velocity in the core. Unless specified, the default value is $M_{\text{core}} = 0$. Note that the choice of driving the system by volumic sources rather than incoming boundary fluxes is arbitrary but was made to offer more flexibility in the driving particle flux distribution.

The situation is slightly different at the outer flux surface ($r = r_{\max}$). Indeed, the absence of particle sink in the system makes it necessary to allow an outgoing flux so as to avoid an infinite increase of the density. Therefore, we impose a normalized density equal to one (the reference density N_0 is then defined as the one at the external edge of the domain) instead of a zero gradient. Concerning the electrostatic potential, the absence of a limiter leads to the absence of a reference potential (role played by the sheath floating potential Λ in the edge version) so that it is necessary to impose an arbitrary value for the potential at the outer boundary. Finally, the following boundary conditions are specified:

$$\begin{aligned} &N(r_{\max} = a) = 1; \quad M(r_{\max} = a) = M_{\text{wall}} \\ &\Phi(r_{\max} = a) = \Phi_{\text{wall}}; \quad \partial_r W(r_{\max} = a) = 0 \end{aligned} \tag{17}$$

M_{wall} characterizing an arbitrary rotation of the outer plasma. By default, Φ_{wall} is chosen equal to the sheath floating potential $\Lambda = -\frac{1}{2}\ln\left[0.5\frac{m_e}{m_i}\left(1+\frac{T_e}{T_i}\right)\right] = -\frac{1}{2}\ln\frac{m_e}{m_i}$ so that the potential field's amplitude is comparable with the one found in the edge version of the code.

In order to insure the numerical stability of previous boundary conditions, it is necessary to damp fluctuations in the vicinity of radial boundaries. Following what was done in Ref. [21], buffer regions are added close to the boundary flux surfaces (within 5 ion ggyro-radii typically), where the parallel resistivity $\eta_\parallel$ is strongly reduced and diffusion coefficients $D_{\perp N/M/W}$ increased. The linear analysis of the *TOKAM-3D* model demonstrates that this parameter modification tends to stabilize the system. This way, fluctuations are damped and diffusion dominates transport processes close to the boundaries, therefore creating a smoothed boundary condition. Buffer regions are also used to make sure that no undesirable flux flows through the boundaries (the code being flux-driven, one wants to control what the actual drive is). To do so, the increase of diffusion coefficients is chosen stronger for diffusion along the poloidal direction than along the radial direction so that buffer regions prevent the development of poloidal gradients which would lead to undesirable drift through the boundaries of the system.

2.4.2. Boundary conditions in the edge/SOL version

Fig. 3 gives an overview of locations where boundary conditions are specified in the edge/SOL version. The difference with the edge version is linked to the presence of the limiter which requires specific boundary conditions and adds a particle sink as well as a reference potential. Buffer regions, also shown in Fig. 3, extend around the limiter.

The toroidal direction φ is still periodic in the whole domain:

$$\forall r,\theta,\varphi \quad X(r,\theta,\varphi+2\pi) = X(r,\theta,\varphi) \tag{18}$$

but it is no more the case for the poloidal direction, the periodicity being lost due to the limiter in the SOL. This way, poloidal periodicity is stated only in the core:

$$\forall r \leqslant a,\theta,\varphi \quad X(r,\theta+2\pi,\varphi) = X(r,\theta,\varphi) \tag{19}$$

In the SOL, Bohm's boundary conditions [34–36] are classically used to model the effect of the sheath at the interface between the limiter and the plasma. In our geometry, field lines intersect the limiter with a non normal pitch angle:

$$\alpha_{\text{inc}} \approx \frac{r}{qR_0} \equiv \epsilon_B \tag{20}$$

Recalling that $u_\perp \ll u_\parallel$, it is nevertheless possible to neglect the contribution of drift velocities in sheath boundary conditions, provided that we do not consider too grazing incidences ($\alpha_{\text{inc}} > 3-4°$). This way, we impose the following boundary conditions at the side plates of the limiter:

$$\begin{aligned} &M(a<r<r_{\max},\theta=-\pi/2\pm\Delta_{\lim}/2) = \mp\sqrt{2} \\ &J_\parallel(a<r<r_{\max},\theta=-\pi/2\pm\Delta_{\lim}/2) = \mp N\sqrt{2}(1-\exp(\Lambda-\Phi)) \end{aligned} \tag{21}$$

where Λ is the sheath floating potential. The presence of the "$\sqrt{2}$" is due to the normalization chosen for the parallel velocity. The condition on the parallel current, coupled to the generalized Ohm's law 8, gives a condition on the parallel derivative of the potential:

$$\nabla_\parallel \Phi = \nabla_\parallel \ln N \pm \eta_\parallel N\sqrt{2}(1-\exp(\Lambda-\Phi)) \tag{22}$$

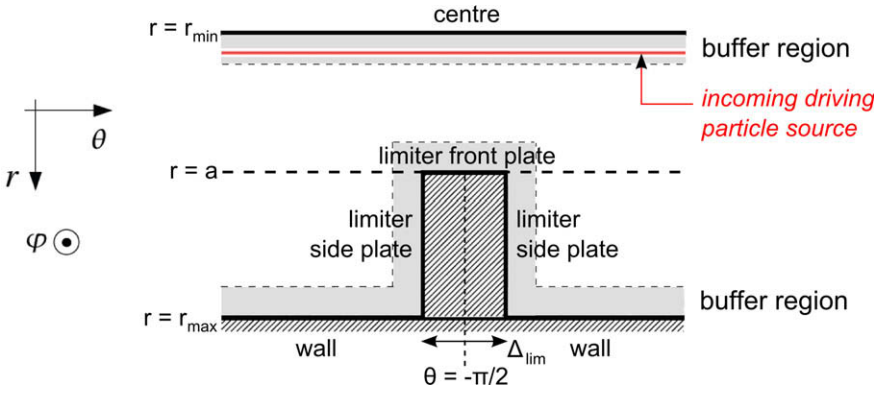

Fig. 3. Localization of boundary conditions, buffer regions and of the core-incoming particle source in the edge/SOL version of *TOKAM-3D* (ploidal section, slab).

It is possible to demonstrate that this non-linear condition is sufficient to determine the potential [37]. We also add a condition on vorticity so as to insure that no current linked to the diffusive term in the charge conservation Eq. (7) leaves or enters the plasma:

$$\partial_\theta W(a < r < r_{\max}, \quad \theta = -\pi/2 \pm \Delta_{\lim}/2) = 0 \tag{23}$$

No particular condition is specified for density.

Boundary conditions at the inner flux surface are the same as in the core version Eq. (16). Contrary to the edge version however, the same conditions can be imposed at the outer flux surface since the potential Φ already has a reference value with the sheath floating potential Λ and that the density is regulated by the parallel particle outflow on the limiter:

$$\begin{aligned} &\partial_r N(r_{\max}) = 0; \quad M(r_{\max}) = M_{\text{wall}} \\ &\partial_r \Phi(r_{\max}) = 0; \quad \partial_r W(r_{\max}) = 0 \end{aligned} \tag{24}$$

The only difference is that M_{wall} is not arbitrarily imposed but is the poloidal distribution corresponding to the analytical solution of the steady-state equilibrium of an isothermal 1D SOL with homogeneous source [34].

Finally, radial boundary conditions are required at $r = a$ at the limiter front plate. In the chosen geometry, field lines are tangential to the wall just in front of the limiter. Bohm boundary conditions are not valid anymore in that case and no clear choice stands out of the literature. In real-world limiter machines, the area of the limiter where field lines are almost tangential (a_{inc}< a few degrees) is very limited and is not expected to have an important influence on the overall behaviour of the plasma. This way, we end-up having to choose boundary conditions for a purely numerical purpose, with the requirement of not constraining the system too much but also of numerical stability. Our treatment relies on a linear interpolation of fields along the poloidal direction between both sides of the limiter. It is detailed in the next section devoted to numerical aspects.

The numerical stability at the transition between open and closed field lines is also insured by the buffer region which extends around the limiter. This stabilization has a price however: the presence of the buffer zone masks physical processes that might take place around the limiter. It is particularly the case for Kelvin–Helmholtz instability that may be expected due to the strong shear on parallel velocity at the LCFS [38]. However, we assume that the presence of the buffer zone influences the system only in its close vicinity, so that the impact of boundary conditions imposed by the limiter on the whole system is correctly modelled.

3. Numerical method

Due to the differences in the geometry and the boundary conditions, the two versions of the previous model do not require the same numerical treatment. In particular, the edge version can take advantage of the periodicity of the poloidal direction while the edge/SOL version has to deal with the presence of the limiter and the discontinuity of boundary conditions at the LCFS. In this section, we first detail the numerical treatment adopted for the edge/SOL version before precising the particularities of the edge version.

3.1. Edge/SOL version

3.1.1. Semi-spectral discretization

The spatial discretization of Eqs. (5)–(8) is performed on the basis of a structured mesh along toroidal coordinates. A semi-spectral scheme is used. Indeed, the toroidal periodicity allows to make use of a treatment in Fourier space along that direction for linear terms:

$$X(r,\theta,\varphi) = \sum_{n_\varphi=-N_\varphi/2}^{N_\varphi/2} \widehat{X}_{n_\varphi}(r,\theta)\exp(in_\varphi\varphi) \tag{25}$$

N_φ being the number of mesh points in the toroidal direction. However, this spectral approach is not possible along the radial and poloidal directions. Along those directions, fourth order finite differences are used. If Δ is the spatial step along the considered direction, the centered discretizations for first and second derivatives at the jth point are:

$$\begin{aligned} f'_j &= \frac{2}{3\Delta}\left[f_{j+1} - f_{j-1} - \frac{f_{j+2} - f_{j-2}}{8}\right] + o(\Delta^4) \\ f''_j &= \frac{1}{12\Delta^2}\left[-30f_j + 16(f_{j+1} + f_{j-1}) - f_{j+2} - f_{j-2}\right] + o(\Delta^4) \end{aligned} \tag{26}$$

The choice of a central differencing scheme rather than an up-winding scheme was made to limit the amount of numerical diffusivity and leave the role of damping small scale structures to well-defined and controlled diffusion terms.

3.1.2. Time-splitting

Three kinds of terms can be distinguished in the system (5)–(8) from the numerical point of view:

(1) Perpendicular diffusion terms:

$$\begin{aligned}\partial_t N &= \cdots + \vec{\nabla}_\perp \cdot \left(D_{\perp N}\vec{\nabla}_\perp N\right)\\ \partial_t M &= \cdots + \vec{\nabla}_\perp \cdot \left(D_{\perp M}\vec{\nabla}_\perp M\right)\\ \partial_t W &= \cdots + \vec{\nabla}_\perp \cdot \left(D_{\perp W}\vec{\nabla}_\perp W\right)\end{aligned} \tag{27}$$

These terms are linear and must be treated implicitly because of the CFL linear stability condition [39] which for large anomalous diffusion coefficients would impose the use of unacceptable small time-steps with an explicit treatment.

(2) Terms linked to the parallel current:

$$\begin{aligned}\partial_t N &= \cdots + B\nabla_\parallel \frac{J_\parallel}{B}\\ \partial_t W &= \cdots + Z\frac{B^3}{N}\nabla_\parallel \frac{J_\parallel}{B}\\ W &= \nabla_\perp^2 \Phi + \frac{\nabla_\perp^2 \ln N}{Z}\\ J_\parallel &= \frac{1}{\eta_\parallel}\nabla_\parallel(\ln N - \Phi)\end{aligned} \tag{28}$$

The parallel resistivity has an extremely low value in typical edge plasma conditions, $\eta_\parallel \sim 10^{-6} - 10^{-5}$ (normalized value). This way, the divergence of the parallel current appears in equations as a diffusion term on $(\ln N - \Phi)$ associated with a dimensionless diffusion coefficient $1/\eta_\parallel$ whose dynamics (electronic) is much faster than the ionic times we are interested in. An implicit approach is therefore compulsory.

(3) other terms:

$$\begin{aligned}\partial_t N &= \ldots - B\nabla_\parallel \frac{NM}{B} - \frac{1}{B}[\Phi, N] - BN\left[\Phi, \frac{1}{B^2}\right] + B\left[N, \frac{1}{B^2}\right] + S_N\\ \partial_t M &= \ldots - M\nabla_\parallel M - \frac{1}{B}[\Phi, M] - (1+Z)\frac{\nabla_\parallel N}{N} - \frac{S_N}{N}M + S_M\\ \partial_t W &= \ldots - M\nabla_\parallel W - \frac{1}{B}[\Phi, W] + (1+Z)\frac{B^3}{N}\left[N, \frac{1}{B^2}\right]\end{aligned} \tag{29}$$

They are mainly non-linear advection terms and source terms. Their dynamics is on an ionic time scale which allows an explicit treatment.

On the basis of this term classification, time-stepping is performed thanks to a time-splitting similar to the one used in Ref. [40]. Let X^{n-1} and X^n be the values of fields at the two last time-steps and $dt = t^n - t^{n-1}$ be the time step width. The next iteration of the fields X^{n+1} is obtained following three sub-steps:

(1) Implicit advancement of perpendicular diffusion terms applied on fields at time $(n-1)$ for a time width dt:

$$\frac{X^\star - X^{n-1}}{dt} = \vec{\nabla}_\perp \cdot \left(D_{\perp X}\vec{\nabla}_\perp X^\star\right) \tag{30}$$

(2) Simultaneous advancement of parallel current terms, advection terms and source terms with a semi-implicit leap-frog scheme:

$$\frac{X^{\star\star} - X^\star}{2dt} = [\text{parallel current terms}]^{\star\star} + [\text{other terms}]^n \tag{31}$$

(3) Implicit advancement of perpendicular diffusion terms applied on fields $X^{\star\star}$ for a time width dt:

$$\frac{X^{n+1} - X^{\star\star}}{dt} = \vec{\nabla}_\perp \cdot \left(D_{\perp X}\vec{\nabla}_\perp X^{n+1}\right) \tag{32}$$

Note that since the leap-frog scheme is unstable due to the decoupling existing between odd and even time-steps, "synchronization" between consecutive time-steps by taking their mean value is regularly necessary:

$$\frac{1}{2}\left(X^n + X^{n+1}\right) \;\Rightarrow\; X^{n+1} \tag{33}$$

A frequency of one synchronization every 30 steps has been found to be a good compromise between stability and precision, even though that may depend on the considered case and no systematic study was carried out. We will now detail each of the steps of the time-splitting.

3.1.3. Perpendicular diffusion terms

Perpendicular diffusion terms 27 take the shape of a 2D Laplacian:

$$\vec{\nabla}_\perp \cdot \left(D_{\perp X}\vec{\nabla}_\perp X\right) = D^r_{\perp X}\partial_{r^2}X + \partial_r D^r_{\perp X}\partial_r X + \frac{1}{r}D^r_{\perp X}\partial_r X + \frac{\cos\theta}{R_0 + r\cos\theta}D^r_{\perp X}\partial_r X + D^\theta_{\perp X}\frac{\partial_{\theta^2}X}{r^2} + \frac{1}{r^2}\partial_\theta D^\theta_{\perp X}\partial_\theta X - \frac{\sin\theta}{R_0 + r\cos\theta}D^\theta_{\perp X}\frac{\partial_\theta X}{r} \tag{34}$$

where $D^r_{\perp X}$ and $D^\theta_{\perp X}$ are the diffusion coefficients for the field X along the radial and poloidal directions ($D^r_{\perp X} \neq D^\theta_{\perp X}$ only in radial buffer regions).

They are advanced with a fully implicit scheme:

$$\frac{X^\diamond - X}{dt} = \vec{\nabla}_\perp \cdot \left(D_{\perp X}\vec{\nabla}_\perp X^\diamond\right) \tag{35}$$

$X^\diamond$ and X referring, respectively to the X field value after and before the application of the diffusion operator on a dt time step. The matrix of the corresponding finite differences linear system is a sparse band ($N_r N_\theta \times N_r N_\theta$) matrix with $4N_\theta$ bandwidth. This system is solved by LU decomposition [39] using the LAPACK library [41]. Since diffusion coefficients are constant and do not depend on the toroidal location, the matrix does not change either and the decomposition is performed only once at the beginning of the execution. The obtained triangular matrices are stored and used at each time step to solve the system.

3.1.4. Parallel current terms

Terms linked to the parallel current 28 constitute the main numerical difficulty of the model. Indeed, they have extremely fast dynamics, which requires an implicit treatment, and couple the three spatial dimensions through the charge balance equation.

In order to avoid a direct inversion of a 3D system, it is possible to modify slightly the system 28 by averaging the two $1/N$ terms along the toroidal direction:

$$\begin{aligned}\partial_t \ln N &= \frac{B}{\langle N\rangle_\varphi}\nabla_\parallel \frac{\frac{1}{\eta_\parallel}\nabla_\parallel(\ln N - \Phi)}{B}\\ \partial_t\left(\nabla^2_\perp \Phi + \nabla^2_\perp \ln N/Z\right) &= Z\frac{B^3}{\langle N\rangle_\varphi}\nabla_\parallel \frac{\frac{1}{\eta_\parallel}\nabla_\parallel(\ln N - \Phi)}{B}\end{aligned} \tag{36}$$

where $\langle N\rangle_\varphi$ is the mean value of the density along the toroidal direction. We also assume that $\eta_\parallel$ is homogeneous along the toroidal direction. This simplification removes potential mode coupling in the toroidal direction, but we assume that such coupling is not a key player of the physics of the system.

If we treat explicitly the $1/\langle N\rangle_\varphi$ terms, the system 36 is now linear in $\ln N$ and Φ with respect to the toroidal direction, which makes it possible to project it in Fourier space following 25. This way, the advancement of parallel current terms is splitted into the resolution of $N_\varphi/2 + 1$ independent 2D ($2N_rN_\theta \times 2N_rN_\theta$) systems along radial and poloidal directions, one for each toroidal wave number n_φ:

$$\begin{aligned}\frac{\widehat{\ln N}^{\star\star}_{n_\varphi} - \widehat{\ln N}^{\star}_{n_\varphi}}{dt} &= \frac{1}{\langle N^\star\rangle_\varphi \eta_\parallel}\left[\nabla^2_\parallel - \frac{\nabla_\parallel}{B}\right]\left(\widehat{\ln N}^{\star\star}_{n_\varphi} - \widehat{\Phi}^{\star\star}_{n_\varphi}\right)\\ \frac{\nabla^2_\perp\left(\widehat{\Phi}^{\star\star}_{n_\varphi} + \widehat{\ln N}^{\star\star}_{n_\varphi}/Z\right) - \nabla^2_\perp\left(\widehat{\Phi}^{\star}_{n_\varphi} + \widehat{\ln N}^{\star}_{n_\varphi}/Z\right)}{dt} &= \frac{ZB^2}{\langle N^\star\rangle_\varphi \eta_\parallel}\left[\nabla^2_\parallel - \frac{\nabla_\parallel}{B}\right]\left(\widehat{\ln N}^{\star\star}_{n_\varphi} - \widehat{\Phi}^{\star\star}_{n_\varphi}\right)\end{aligned} \tag{37}$$

with $\nabla_\parallel = 1/R_0(in_\varphi - \partial_\theta/q)$. Each of these systems is solved by LU decomposition using the direct sparse solver MUMPS [42,43] rather than LAPACK. Indeed, although these matrices have the same structure as the ones obtained from the discretization of diffusion terms (sparse band), they couple several fields (the density N, the potential Φ and eventually the temperatures T_e and T_i in future versions) hence leading to unacceptably larger memory requirements if a dense solver were used. Thus, MUMPS allows for an optimization of the memory usage. Since the matrix evolves with the time step and the toroidal wave number, decomposition and resolution must be performed at each step but the analysis of the matrix structure (the pattern of non-zero elements) is called once for all at the beginning of the execution.

3.1.5. Advection and source terms

These terms can be treated explicitly and are included as second-hand side in the system on parallel current terms. They are first computed in real space by finite differences before being projected in Fourier space using the FFTW library [44]. Once the system has been solved, anti-aliasing filtering is applied before returning to real space.

3.1.6. Boundary conditions around the limiter

Special care has been given to boundary conditions around the limiter. In particular, the treatment of radial boundary conditions at $r = a$ in the poloidal angular sector of the limiter is of primary importance for the stability of the scheme.

Fig. 4 illustrates the discretization strategy we have adopted around the limiter. In the open field lines region ($r > a$), uncentered finite differences are used when necessary (at surfaces 1 and 2 in Fig. 4) to compute derivatives along the poloidal direction. For surface 1, the following developments are used:

$$\begin{aligned} f_1' &= \frac{1}{\Delta}\left[-\frac{25}{12}f_1 + 4f_2 - 3f_3 + \frac{4}{3}f_4 - \frac{1}{4}f_5\right] + o(\Delta^4) \\ f_2' &= \frac{1}{\Delta}\left[-\frac{1}{4}f_1 - \frac{5}{6}f_2 + \frac{3}{2}f_3 - \frac{1}{2}f_4 + \frac{1}{12}f_5\right] + o(\Delta^4) \\ f_1'' &= \frac{1}{\Delta^2}\left[\frac{35}{12}f_1 - \frac{26}{3}f_2 + \frac{19}{2}f_3 - \frac{14}{3}f_4 + \frac{11}{12}f_5\right] + o(\Delta^4) \\ f_2'' &= \frac{1}{\Delta^2}\left[\frac{11}{12}f_1 - \frac{5}{3}f_2 + \frac{1}{2}f_3 + \frac{1}{3}f_4 - \frac{1}{12}f_5\right] + o(\Delta^4) \end{aligned} \tag{38}$$

indexes 1 and 2 referring to the two mesh points that are the closest to the limiter along the poloidal direction, for given radial and toroidal positions. The symmetric developments are used on the other side (surface 2). The use of the same kind of uncentered discretization for radial derivatives in the closed field lines region in front of the limiter (surface 3 in Fig. 4) leads to the appearance of spurious oscillations responsible for the crash of the time-stepping. As stated in section 2.4.2, the choice of boundary conditions at that location can be driven solely by numerical considerations. We have therefore solved the problem by using centered discretizations for the radial derivatives, based on the use of virtual points inside the limiter which are computed by linear interpolation along the poloidal direction between both lateral plates of the limiter. Fig. 4 illustrates the principle. This insures a smooth correlation between the fields in front of the limiter and their values on both sides of it just out of the LCFS, thus solving stability issues.

Let us now detail further the treatment of the current boundary condition at the limiter plates in the SOL. This boundary condition, expressed in 22 as a condition on the parallel gradient of the electrostatic potential Φ, is strongly non-linear due to the presence of the exponential. A purely explicit treatment of this exponential is not possible since an implicit reference to the $\Lambda - \Phi$ term is necessary to remove the undetermination on the amplitude of the potential in the whole domain. So as to allow an implicit approach, we have linearized Eq. 22 under the assumption that the fields evolve slowly compared to the time step:

$$\frac{1}{\eta_\parallel}\nabla_\parallel\left(\ln N^{n+1} - \Phi^{n+1}\right) = \pm N^n\sqrt{2}(1 - \exp(\Lambda - \Phi^n)) \pm \langle N^n\sqrt{2}\exp(\Lambda - \Phi^n)\rangle_\varphi\left(\Phi^{n+1} - \Phi^n\right) \tag{39}$$

the exponents n and $n + 1$ standing respectively for the previous time step and the next one. Note that the coefficient of the implicit right-hand side term has been averaged along the toroidal direction to comply with the treatment in Fourier space. This expansion remains valid as long as $\Phi^{n+1} - \Phi^n/T_e \ll 1$ and $\widetilde{\Phi}/T_e \ll 1$, $\widetilde{\Phi}$ is the toroidally fluctuating component of Φ.

3.1.7. Parallelization

A rough parallelization of the code has been implemented for the most time-consuming parts of the above scheme, ie the implicit treatment of the terms linked to the parallel current and the inversion of the diffusion terms.

Diffusion terms act only along perpendicular directions. It is therefore possible to treat independently each poloidal plane of our mesh and to split them on different processes.

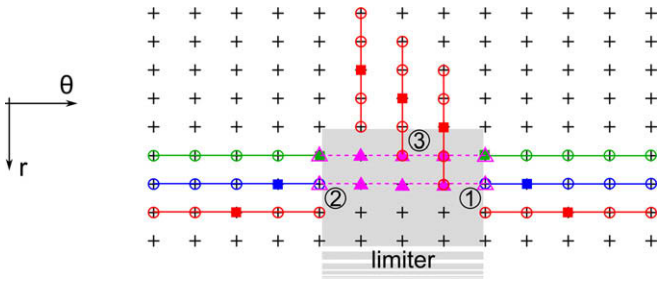

Fig. 4. Adopted discretization for the computation of derivatives around the limiter. Filled squares indicate the points where derivatives are computed; empty circles they are linked to indicate the discretization points used for the computations of the derivative. Filled triangles are virtual points inside the limiter. They are computed by linear interpolation along the poloidal direction between the two points located on each side of the limiter and represented by empty triangles.

As for parallel current terms, they are naturally split in the Fourier space, which allows distributing the $N_\varphi/2+1$ independent Fourier modes among N_g grapes of $N_{p/g}$ processes. Each grape manages a subset of toroidal modes using the parallel inversion tool provided by MUMPS, before broadcasting the updated value of the unknown fields to the other processes.

Communication management is done with MPI. Up to now, the code has never been run on massively parallel architectures and parallel execution has been limited to a maximum number of 8 processes. No systematic analysis of the performance of this parallelization has been carried out. We can however quote that a case with $N_g = 4$ grapes of $N_{p/g} = 1$ processor and with $N_\varphi = 64$ runs around 3.2 times faster than the equivalent mono-processor case.

3.2. Edge version

The scheme applied in the edge version of the code differs slightly from the one described here-above. Taking advantage of the periodicity in θ, projection in Fourier space can be extended to the poloidal direction:

$$X(r,\theta,\varphi) = \sum_{m_\theta,n_\varphi} \widehat{X}_{m_\theta,n_\varphi}(r)\exp(im_\theta\theta + in_\varphi\varphi) \tag{40}$$

provided we consider several supplementary simplifying assumptions.

Concerning diffusion terms, diffusion coefficients are required to depend only on the radial position r and the θ dependence of the Laplacian operator also has to be neglected:

$$\vec{\nabla}_\perp\cdot\left(D_{\perp X}\vec{\nabla}_\perp X\right) = D^r_{\perp X}\partial_{r^2}X + \partial_r D^r_{\perp X}\partial_r X + \frac{1}{r}D^r_{\perp X}\partial_r X + D^\theta_{\perp X}\frac{\partial_{\theta^2}X}{r^2} \tag{41}$$

Under these assumptions, each Fourier mode is decoupled from the others and the treatment of diffusion terms is reduced to the inversion of $N_\varphi \times (N_\theta/2+1)$ band matrices representing 1D complex Laplacians.

In a same way, the use of Fourier projection along the poloidal direction for parallel current terms simplifies the numerical problem only if poloidal modes can be treated independently. This requires a further simplification of the system 37:

$$\begin{aligned}
&\frac{\widehat{\ln N}^{\star\star}_{m_\theta,n_\varphi} - \widehat{\ln N}^{\star}_{m_\theta,n_\varphi}}{dt} = \frac{1}{\langle N^n\rangle_{\theta,\varphi}\eta_\parallel}\left[\nabla^2_\parallel - \frac{\nabla_\parallel}{\langle B\rangle_\theta}\right]\left(\widehat{\ln N}^{\star\star}_{m_\theta,n_\varphi} - \widehat{\Phi}^{\star\star}_{m_\theta,n_\varphi}\right)\\
&\frac{\nabla^2_\perp\left(\widehat{\Phi}^{\star\star}_{m_\theta,n_\varphi} + \widehat{\ln N}^{\star\star}_{m_\theta,n_\varphi}/Z\right) - \nabla^2_\perp\left(\widehat{\Phi}^{\star}_{\theta,n_\varphi} + \widehat{\ln N}^{\star}_{m_\theta,n_\varphi}/Z\right)}{dt} = \frac{Z\langle B^2\rangle_\theta}{\langle N^n\rangle_{\theta,\varphi}\eta_\parallel}\left[\nabla^2_\parallel - \frac{\nabla_\parallel}{\langle B\rangle_\theta}\right]\left(\widehat{\ln N}^{\star\star}_{m_\theta,n_\varphi} - \widehat{\Phi}^{\star\star}_{m_\theta,n_\varphi}\right)
\end{aligned} \tag{42}$$

the average values now being taken along flux surfaces, not only the toroidal direction. $\eta_\parallel$ should also depend only on r. In such conditions, the implicit advancement consists in inverting $\propto N_\theta \times N_\varphi$ dense band systems of size $\propto N_r$ (instead of $\propto N_\varphi$ sparse band systems of size $\propto N_r \times n_\theta$) which leads to a substantial acceleration of the treatment. The density of the band matrices allows using LAPACK instead of MUMPS for the LU decomposition.

The advancement scheme itself is also slightly different from the edge/SOL version, taking advantage of the fact that the inversion of the parallel current terms' operators is now far less time-consuming. The time-splitting is centered around a predictor–corrector scheme instead of a leap-frog scheme, so that the advancement procedure to the $(n+1)$th time step is the following:

(1) Implicit advancement of perpendicular diffusion terms applied on fields at time n for a time width $dt/2$:

$$\frac{X^\star - X^n}{dt/2} = \vec{\nabla}_\perp\cdot\left(D_{\perp X}\vec{\nabla}_\perp X^\star\right) \tag{43}$$

(2) Simultaneous advancement of parallel current terms, advection terms and source terms with a semi-implicit predictor–corrector scheme, with a predictor step:

$$\frac{X^\triangleright - X^\star}{dt} = [\text{parallel current terms}]^\triangleright + [\text{other terms}]^\star \tag{44}$$

followed by a corrector one:

$$\frac{X^{\star\star} - X^\star}{dt} = [\text{parallel current terms}]^{\star\star} + [\text{other terms}]^\triangleright \tag{45}$$

(3) Implicit advancement of perpendicular diffusion terms applied on fields $X^{\star\star}$ for a time width $dt/2$:

$$\frac{X^{n+1} - X^{\star\star}}{dt} = \vec{\nabla}_\perp\cdot\left(D_{\perp X}\vec{\nabla}_\perp X^{n+1}\right) \tag{46}$$

Such a choice makes it necessary to advance parallel current terms twice per time step (compared to once with the leap-frog), but does not require anymore the use of arbitrary synchronizations between odd and even time-steps to insure its stability.

3.3. Performance

A very brief study of performances has been performed. The evolution of the computation time for each time step as a function of the number of mesh points is given in Fig. 5 for the both versions. These curves show as expected a quasi-linear evolution with the number of points in each direction, except for the N_θ dependence in the edge/SOL version. We can notice however that this dependence is slightly weaker than N_θ^2 whereas we might expect an evolution in N_θ^3 due to the parallel current terms. Indeed, the size of the corresponding band matrix and its bandwidth are both proportional to N_θ, so that a dense band LU decomposition/inversion would evolve in $size \times bandwidth^2 \propto N_\theta^3$. This shows the efficiency of the use of MUMPS instead of LAPACK for the treatment of these terms. Note that we get a better (linear) dependence in N_θ in the Edge version because the matrices obtained in that case are dense band matrices whose bandwidth does not depend on N_θ.

4. Verification and physical cases

We will now illustrate the usage of *TOKAM-3D*. In the following section, we present typical physical applications of both versions of the code as well as some verifications performed on the basis of these cases.

4.1. Parallel transport

Let us start with a verification linked to the choice of a structured mesh along (θ, φ). Indeed, the physics of transport in a magnetized plasma is strongly anisotropic, the magnetic field's direction playing a specific role in transport processes. In the frame of our approach however, operators acting along the parallel direction appear as combinations of operators along θ and φ and, even though the choice of a structured mesh in (θ, φ) facilitates the numerical treatment of the toroidal geometry, the correct description of the parallel dynamics is not insured.

In order to address this issue, we have run a simulation solving only the minimal set of equations describing parallel transport:

$$\partial_t N + \nabla_\parallel (NM) = 0 \tag{47}$$

$$\partial_t M + M \nabla_\parallel M = -\frac{\nabla_\parallel N}{N} \tag{48}$$

The considered case consisted in studying the evolution of an homogeneous plasma seeded with a density blob localized along θ and φ. Fig. 6 shows the density at $t = 0$, $t = 6000/\omega_{ci}$ and $t = 2.10^5/\omega_{ci}$ for two flux surfaces with different safety factors q. The observed behaviour is conform to what suggests the analytical resolution of such a system [45]: the density peak splits into two symmetric peaks propagating in opposite direction along the field line with quasi-acoustic velocities. After a few transit times, the blobs can end-up at the same position and interact as can be seen in the $t = 2 \times 10^5/\omega_{ci}$ window of the

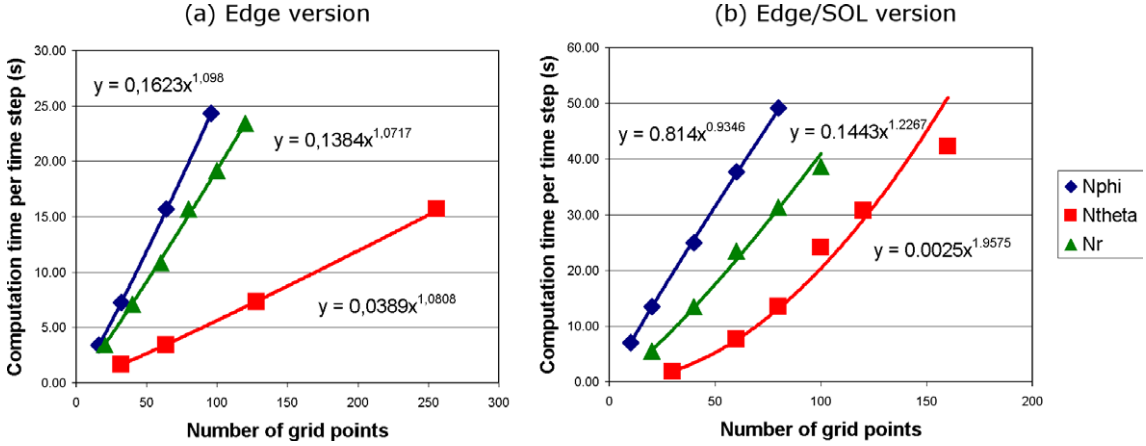

Fig. 5. Computation time per time-step as a function of the number of mesh points along each direction for the edge version of *TOKAM-3D* (a) and the edge/SOL version (b). The default values for the mesh size (when not varied as the plotting parameter) are: $N_r = 80$, $N_\theta = 256$ and $N_\varphi = 64$ for the edge version and $N_r = 40$, $N_\theta = 80$ and $N_\varphi = 20$ for the edge/SOL version.

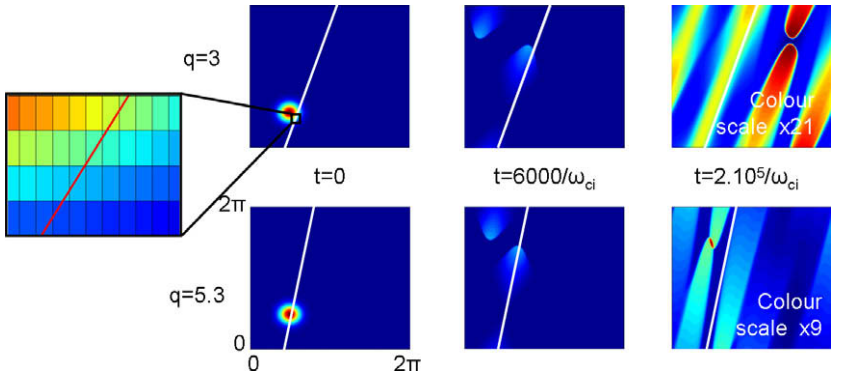

Fig. 6. Temporal evolution of an initial density blob at 2 different radii corresponding to 2 different values of the safety factor q: top $q = 3$, bottom $q = 5.3$. The left picture shows a zoom on the unaligned structured mesh compared to the direction of a field line.

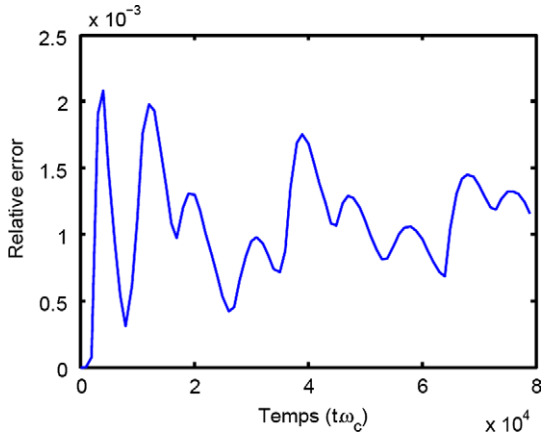

Fig. 7. Temporal evolution of the relative error on particle balance during the parallel advection of the blobs in the case shown in Fig. 6.

$q = 5.3$ flux surface. As shown in Fig. 7, the relative error on particle balance during the parallel advection of the blobs remains lower than 0.5% over several ion parallel transit times (of the order of $2.10^4/\omega_{ci}$ in that case). These results demonstrate that the choice of a non-aligned structured mesh does not prevent a correct treatment of the parallel dynamics.

4.2. Edge/SOL version in laminar regime

We now return to the full *TOKAM-3D* model and consider a case run with the following parameters:

$$\begin{aligned} &N_r = 80 \quad N_{rSOL} = 40 \quad N_\theta = 160 \quad N_\phi = 40 \\ &r_{\min} = 50 \quad a = 100 \quad R_0/a = 3.4 \quad \Delta_{\lim} = \pi/8 \\ &\eta_\parallel = 1 \times 10^{-6} \quad D_{\perp N} = D_{\perp M} = D_{\perp W} = 6 \times 10^{-1} \end{aligned} \tag{49}$$

the normalization convention being the one stated in section 2.3 (for example, the diffusion coefficients are normalized to $\rho_L^2.\omega_{ci}$ so that anomalous transport coefficients are of the order of *1* and classical transport coefficients are of the order of 10^{-2}). Since the number of radial grid points in the SOL N_{rSOL} is not equal to zero, it is the edge/SOL version of the code which is used, with $r_{\max} = a + \frac{N_{rSOL}}{N_r - N_{rSOL} - 1}(a - r_{\min}) \approx 151$. The volumic source term S_N takes the form of a radial gaussian and is located in the inner buffer region so as to account for an incoming particle flux from the core.

The values chosen for diffusion coefficients correspond to anomalous transport coefficients. Along with the average value imposed for the incoming particle source, we expect the simulated plasma to be stable with respect to small scale turbulence, which can also be confirmed by a linear analysis of the system (5)–(8). However, large scale structures linked to the existence of global drifts, curvature and the presence of the limiter are still modelled. In such a regime, that we will refer to as "laminar", *TOKAM-3D* is used simply as a 3D global transport code.

Fig. 8 shows the obtained radial density profile. As stated above, the plasma remains stable and the steady-state equilibrium, which is reached in a few confinement times, is toroidally symmetric. Currents in the plasma and at the sheaths also

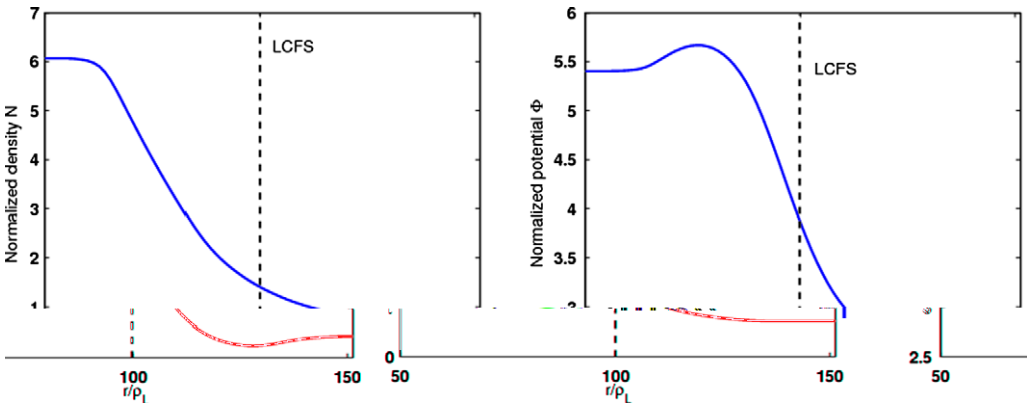

Fig. 8. Steady-state radial profiles for the density N (left) and electrostatic potential Φ (right). The equilibrium is toroidally symmetric.

evolve towards an equilibrium which determines the spatial distribution of the electrostatic potential Φ. This way, a potential profile develops in the plasma (Fig. 8), fully consistently driven by boundary conditions on currents and the charge balance Eq. 7, and is responsible for a global ExB drift along the poloidal direction.

An interesting verification of the right behaviour of the code can be obtained when looking at the poloidal equilibrium of the electrostatic potential Φ and of the parallel current $J_{\parallel}$. In the closed field lines region, the non-zero divergence of the diamagnetic current is responsible for a vertical charge separation in the presence of the radial density gradient. The resulting $m_\theta = 1$ mode on the potential has the following expression

$$\Phi = \eta q^2 R_0^2 \partial_r N \sin\theta \tag{50}$$

and drives equatorial parallel currents, the so-called Pfirsh–Schlüter currents, which counterbalance the charge separation and have the following dependence. These features can be observed in our simulation results (Fig. 9) and show excellent agreement with the analytically expected phase and amplitude. In the open field lines region, the poloidal dependence of the potential is mainly determined by sheath boundary conditions as well as the density distribution. In particular, the poloidal potential profile drops in the vicinity of the limiter along with the density. This behaviour can also be observed in Fig. 9. The analytically expected parallel equilibrium (using simulated perpendicular terms as parameters) is also shown and agrees extremely well.

4.3. Edge version in turbulent regime

If we progressively decrease the diffusion coefficients but keep the incoming particle flux constant, the radial density gradient, which is a destabilizing factor, steepens while the stabilizing effect of the diffusive damping rate vanishes. Perpendic-

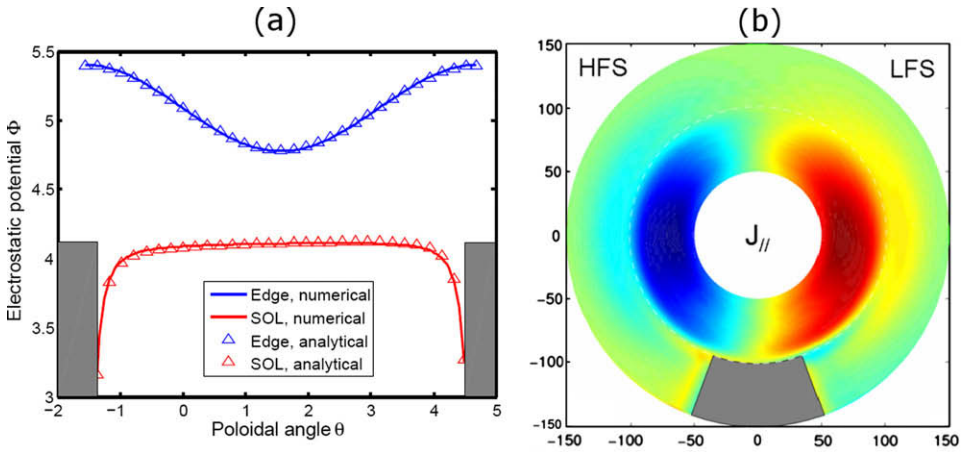

Fig. 9. (a) equilibrium poloidal profiles of the electrostatic potential in the SOL and in the closed field lines region in laminar regime, showing comparison with the analytically calculated equilibrium; (b) poloidal section of the steady-state parallel current distribution exhibiting Pfirsch–Schlüter currents.

ular transport then becomes dominated by small scale fluctuations. When used in this regime, *TOKAM-3D* is a global flux-driven turbulent code without scale separation.

To illustrate this aspect of the code, let us consider a simulation run with the following parameters:

$$\begin{aligned} &N_r = 80 \quad N_{rSOL} = 0 \quad N_\theta = 250 \quad N_\phi = 64 \\ &r_{\min} = 120 \quad a = 200 \quad R_0/a = 3.4 \\ &\eta_\parallel = 3 \times 10^{-5} \quad D_{\perp N} = D_{\perp M} = D_{\perp W} = 2 \times 10^{-2} \end{aligned} \tag{51}$$

The edge version of the code is used since no mesh point is specified in the SOL (N_{rSOL}).

Fig. 10 shows a poloidal section of the density once the equilibrium has been reached. This equilibrium is not static and is characterized by strong fluctuations of all the modelled fields, but the time averaged values have reached a steady-state. The radial profiles of the mean convective turbulent flux

$$\Gamma_r^{\text{turb}} = -\left\langle N \frac{1}{r} \frac{\partial_\theta \Phi}{B} \right\rangle_{t,\theta,\varphi} \tag{52}$$

and mean diffusive flux

$$\Gamma_r^{\text{diff}} = -\langle D_{\perp N} \partial_r N \rangle_{t,\theta,\varphi} \tag{53}$$

are also given and demonstrate that perpendicular transport is strongly dominated by turbulent processes, except in buffer regions where the rise of diffusion coefficients stabilizes fluctuations.

An important verification of first principle based transport codes is the verification of balance laws. Matter balance over an arbitrary volume of the simulation box is given in Fig. 11. But for a peak around 10% at the first relaxation, the relative error remains lower than 5% with a typical value of 3%, which is a good accuracy compared with usual results.

Another verification with the code run in turbulent regime concerns linear growth rates. Fig. 12 shows a comparison of the numerical and analytical growth rates of poloidal modes for the interchange instability, using a simplified version of the model [16]:

$$\partial_t N + [\Phi, N] = D_{\perp N} \nabla_\perp^2 N + S_N \tag{54}$$

$$\partial_t \nabla_\perp^2 \Phi + \left[\Phi, \nabla_\perp^2 \Phi\right] = -g \frac{1}{r} \partial_\theta \ln N + D_{\perp W} \nabla_\perp^4 \Phi \tag{55}$$

Excellent agreement is found, which validates the advancement scheme and particularly the time-splitting we have adopted.

4.4. Edge/SOL version in turbulent regime

The edge version of *TOKAM-3D* is the adapted choice for edge turbulence studies which do not require taking into account the presence of the limiter since it is less time-consuming than the edge/SOL version. However, as soon as closed field lines have to be addressed, it is necessary to use the edge/SOL version of the code.

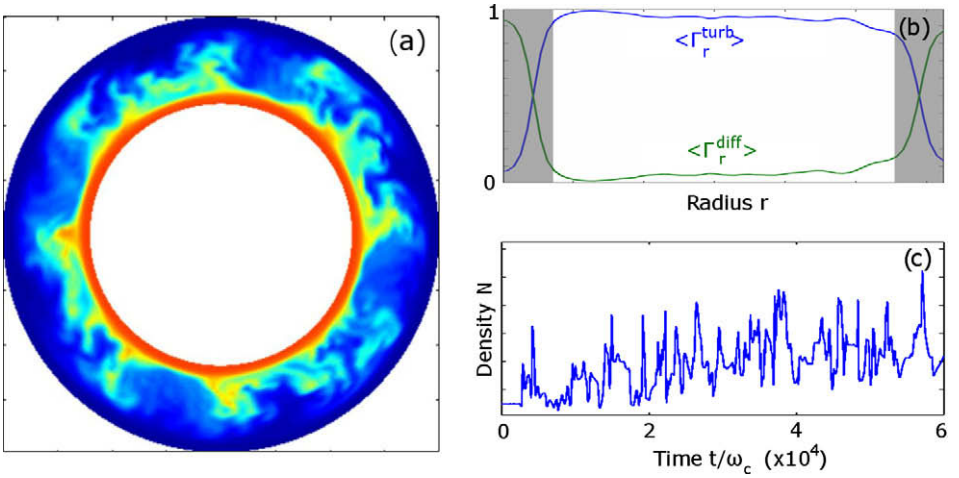

Fig. 10. (a) Poloidal section of the density in non-linear turbulent regime; (b) comparison of the radial flux profiles due to turbulent convective processes and diffusion. The radial extension of buffer zones corresponds to the shaded areas; (c) temporal plot of the density at the bottom of the machine at $r - r_{\min} = (a - r_{\min})/2$.

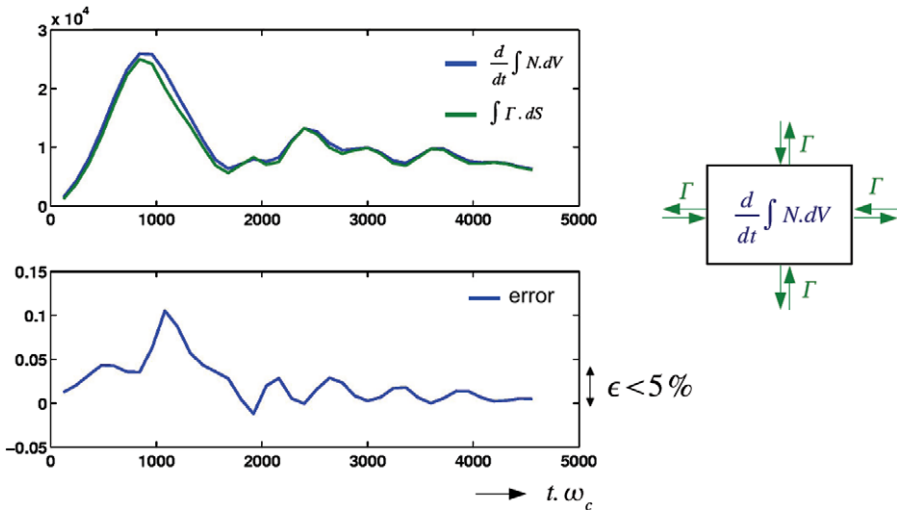

Fig. 11. Top: comparison between the temporal variation of the total amount of matter inside an arbitrary volume and the integral of incoming and outgoing particle fluxes at its boundaries. Bottom: relative error.

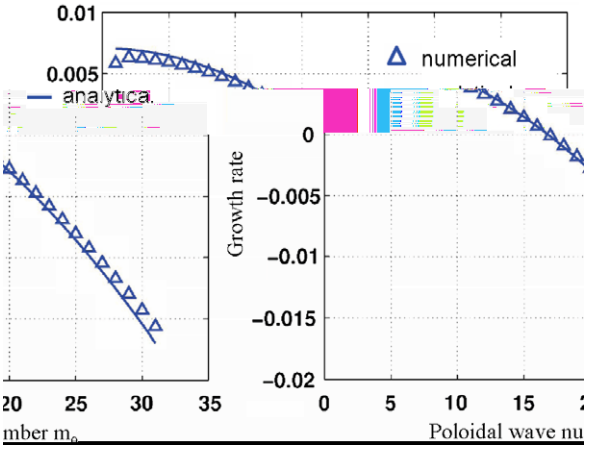

Fig. 12. Comparison of the numerically obtained linear growth rate and the analytical one for the interchange instability.

To finish our quick overview of the field of application of *TOKAM-3D*, let us consider a simulation run in turbulent regime with the edge/SOL version:

$$\begin{aligned} &N_r = 80 \quad N_{rSOL} = 50 \quad N_\theta = 260 \quad N_\phi = 60 \\ &r_{\min} = 50 \quad a = 100 \quad R_0/a = 3.4\Delta_{\lim} = \pi/26 \\ &\eta_\parallel = 1 \times 10^{-4} \quad D_{\perp N} = D_{\perp M} = D_{\perp W} = 6 \times 10^{-2} \end{aligned} \tag{56}$$

The initially stable density gradient tends to steepen as the incoming particle source fuels the system, until first unstable modes appear and trigger a transition towards turbulent regime. As shown in Fig. 13, density structures appear in the vicinity of the LCFS and propagate outward in the SOL. Their amplitude is more important on the low field side than on the high field side of the poloidal section which indicates an interchange-like mechanism. The clear influence of the q profile is visible from the poloidal deformation the density structures exhibit as they travel outward in the SOL, particularly at the inner midplane.

Some comments must be made concerning the obtention of the previous case. The first relaxation of the plasma generates structures characterized by shorter gradient lengths and larger propagation velocities than those observed once the non-linear saturated regime is reached. This phase of the simulation is therefore particularly sensitive to numerical instabilities and makes it necessary to run the code with time-steps 4–5 times smaller than the ones used in the rest of the simulation, which strongly penalizes the execution time. The use of a shock capturing scheme for convection terms might solve this drawback and is considered for future development of the code.

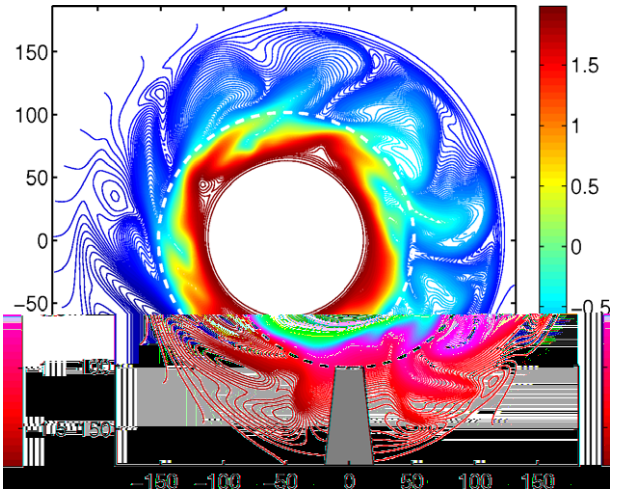

Fig. 13. Poloidal section of the density at the end of the first turbulent relaxation (logarithmic colour scale).

5. Summary

A new edge transport and turbulence code, named *TOKAM-3D*, has been developed. This flux-driven code solves 3D fluid drift equation in a global toroidal geometry without assuming any scale separation. It therefore allows analysing the interaction between large scale structures and the smallest turbulent eddies. Two versions of the code have been developed: the first one, designated as the edge version, is able to treat exclusively closed field lines just inside the Last Closed Flux Surface (LCFS); the second one, the so-called edge/SOL version, can address both closed and open field lines across the LCFS in limiter configuration. Plasma–wall interaction appears when necessary through Bohm boundary conditions on the parallel velocity and current. Time-splitting is used for the numerical advancement of both versions, but each numerical scheme has specific features so as to be adapted to the modelled geometry.

A quick overview of the field of application of the code based on simple physical cases has also been presented. The code can in particular be run in a continuum of transport regimes ranging from purely diffusive transport (it is then used as a global transport code) to purely turbulent regime just by acting on input parameters. Several verifications have been performed on these simulations. The choice of a non-aligned structured mesh does not prevent a right description of the parallel dynamics and good accuracy is obtained for matter conservation or the growth rates of instabilities. Some limitations subsist concerning the numerical stability of large transient convective events, which makes it demanding from the computation time point of view to go through the first turbulent relaxation with the edge/SOL version. However, even though the physics included in the code remains simpler than what is modelled in some other tools, the current versions of TOKAM-3D can already address a wide range of physical issues [46] and constitute a first step in a long term project for the modelling of the edge plasma.

References

[1] A. Loarte et al, Nuclear Fusion 47 (2007) S203.
[2] B. LaBombard et al, Nuclear Fusion 44 (2004) 1047.
[3] C.P. Ritz et al, Physics Review Letters 62 (1989) 1844.
[4] G.A. Hallock, A.J. Wootton, R.L. Hickok, Physics Review Letters 59 (1987) 1301.
[5] T.T. Ribeiro, B. Scott, Plasma Physics and Controlled Fusion 47 (2005) 1657.
[6] B.D. Dudson et al, Plasma Physics and Controlled Fusion 50 (2008) 124012. 9pp.
[7] F. Wagner et al, Physics Review Letters 49 (1982) 1408.
[8] A. Leonard, Journal of Physics Conference Series 123 (2008) 012001.
[9] J. Rice et al, Nuclear Fusion 39 (1999) 1175.
[10] T. Rognlien, J. Milovich, M. Rensink, G. Porter, Journal of Nuclear Materials 196–198 (1992) 347.
[11] A. Chankin et al, Contribution to Plasma Physics 40 (2000) 288.
[12] B.J. Braams, P.J. Harbour, M.F.A. Harrison, E.S. Hotston, J.G. Morgan, Journal of Nuclear Materials 121 (1984) 75.
[13] A. Runov et al, Contribution to Plasma Physics 42 (1984) 169.
[14] V. Naulin, Journal of Nuclear Materials 363–365 (2007) 24.
[15] G.Y. Antar, G. Counsell, Y. Yu, B. Labombard, P. Devynck, Physics of Plasmas 10 (2003) 419.
[16] Y. Sarazin, P. Ghendrih, Physics of Plasmas 5 (1998) 4214.
[17] N. Bisai et al, Physics of Plasmas 11 (2004) 4018.
[18] O.E. Garcia, V. Naulin, A.H. Nielsen, J.J. Rasmussen, Physics of Plasmas 12 (2005) 062309.
[19] Y. Sarazin et al, Journal of Nuclear Materials 313–316 (2003) 796.
[20] R.E. Waltz et al, Physics of Plasmas 4 (1997) 2482.
[21] P. Beyer et al, Plasma Physics and Controlled Fusion 49 (2007) 507.
[22] T. Rognlien, M. Umansky, X. Xu, R. Cohen, L. LoDestro, Journal of Nuclear Materials 337–339 (2005) 327. PSI-16.

[23] X.Q. Xu, W.M. Nevins, R.H. Cohen, T.D. Rognlien, M.V. Umansky, Contributions to Plasma Physics 44 (2004) 105.
[24] Y. Nishimura, K. Borrass, D. Coster, B. Scott, Contributions to Plasma Physics 44 (2004) 194.
[25] X.Q. Xu, R.H. Cohen, T.D. Rognlien, J.R. Myra, Physics of Plasmas 7 (2000) 1951.
[26] X.Q. Xu, W.M. Nevins, R.H. Cohen, T.D. Rognlien, M.V. Umansky, Contribution to Plasma Physics 44 (2004) 105.
[27] X.Q. Xu, M.V. Umansky, B. Dudson, P.B. Snyder, Communication and Computer Physics 4 (2008) 949.
[28] B. Scott, in: The 41st Annual Meeting of the Division of Plasma Physics of the American Physical Society, vol. 7, 2000, p. 1845.
[29] R. Cohen et al, Nuclear Fusion 47 (2007) 612.
[30] J.R. Myra, D.A. D'Ippolito, X.Q. Xu, R.H. Cohen, Physics of Plasmas 7 (2000) 2290.
[31] S. Braginskii, in: M.A. Leontovich (Ed.), Transport Processes in a Plasma, Reviews of Plasma Physics, vol. 1, Consultant Bureau, New York, 1965.
[32] B. Scott, Low frequency fluid drift turbulence in magnetized plasmas, IPP 5/92, 2001.
[33] F.L. Hinton, C.W. Horton, Physics of Fluids 14 (1971) 116.
[34] P.C. Stangeby, The plasma boundary of magnetic fusion devices, IOP, 2000.
[35] R. Chodura, Physics of Fluids 25 (1982) 1628.
[36] R.H. Cohen, D. Ryutov, in: The 40th Annual Meeting of the Division of Plasma Physics of the American Physical Society, vol. 6, 1999, p. 1995.
[37] C. Negulescu, A. Nouri, P. Ghendrih, Y. Sarazin, Kinetic and Related Models 1 (2008) 619.
[38] X. Garbet, C. Fenzi, H. Capes, P. Devynck, G. Antar, Physics of Plasmas 6 (1999) 3955.
[39] W.H. Press, W.T. Vetterling, S.A. Teukolsky, B.P. Flannery, Numerical Recipes: The Art of Scientific Computing, Cambridge University Press, 2007.
[40] V. Grandgirard et al, Journal of Computational Physics 217 (2006) 395.
[41] E. Anderson et al., LAPACK Users' Guide, third ed., Society for Industrial and Applied Mathematics, Philadelphia, PA, 1999.
[42] P. Amestoy, I. Duff, J.-Y. L'Excellent, Computational Methods in Applied Mechanics and Engineering 184 (2000) 501.
[43] P. Amestoy, I. Duff, J. Koster, J.-Y. L'Excellent, SIAM Journal of Matrix Analysis and Applications 23 (2001) 15.
[44] M. Frigo, S. Johnson, Proceedings of the IEEE 93 (2) (2005) 216.
[45] R. Leveque, Numerical Methods for Conservation Laws, Birkhaüser, 1992.
[46] P. Tamain et al, Journal of Nuclear Materials 390–391 (2009) 347.